

Bifurcations and transport barriers in the resistive- g paradigm

M. Berning and K. H. Spatschek

Institut für Theoretische Physik, Heinrich-Heine-Universität Düsseldorf, D-40225 Düsseldorf, Germany

(Received 5 October 1999; revised manuscript received 9 December 1999)

The so-called resistive- g (resistive pressure-gradient-driven turbulence) paradigm is a widely accepted and frequently investigated model for nonlinear plasma dynamics. The parameter dependences of the generated transport barriers as well as third order bifurcations will be discussed numerically and analytically in the present paper. First, using a Galerkin representation, bifurcating states (from the conductive states in a rectangular cell) are investigated for the cases when only one unstable mode dominates. The dependence of the bifurcation properties on the aspect ratio of the domain is discussed, leading to the conclusion that for vanishing (or small) magnetic shear the so-called low, high, and edge localized mode transitions do not occur for small aspect ratios of the domain. Including reasonable magnetic shear, the small-aspect-ratio cutoff disappears, and transport barriers may exist in a broad parameter range. Second, for small aspect ratios, interesting codimension-2 bifurcations occur. When unfolding the dynamics up to third order, e.g., a weakly nonlinear interaction of convection cells is observed. The analytical results are confirmed by numerical simulations.

PACS number(s): 52.35.Py, 47.20.Ky, 52.55.-s

I. INTRODUCTION

In complex physical systems, e.g., magnetically confined plasmas, various physical processes exist and interact simultaneously [1]. A complete and detailed theory of such multifaceted systems will not be possible in the near future. The so-called reduced models turned out to be extremely helpful in analyzing specific phenomena. The advantages of reduced models, which follow from quite complicated transport equations, were already recognized a long time ago in fluid theory. For example, the Boussinesq equations [2] are assumed to be good model equations for the Rayleigh-Bénard (RB) problem. In plasma physics, the so-called reduced magnetohydrodynamic (MHD) equations [3,4] proved their enormous potential for applications during the last decade. While the original reduced MHD models were developed for single-fluid MHD with fast motion (on the scale of the thermal velocities), for slower motion a reduction of the two-fluid plasma equations was necessary. The latter reduction has also been successfully performed [5], leading, e.g., to the so-called resistive- g paradigm (RGP). Here g stands for an effective field (e.g., caused by field line curvature), in analogy to the gravitational field in classical hydrodynamical applications.

The two-dimensional (2D) Boussinesq equations (2DB) and the RGP equations [6] (for a plasma in the limit of vanishing parallel electric conductivity and a shear-free magnetic field) are very prominent reduced models of similar forms. The RGP is being used to describe the generation of transport barriers. The latter are believed to be responsible for the transition between different confinement modes in magnetically confined plasmas: low (L), high (H), as well as edge localized modes (ELMs) [7], respectively. On the other hand, the 2DB equations describe similar transport modification processes for the RB convection (see, e.g., [8]).

In their simplest versions, RB convection, on the one hand, and velocity shear flow generation in plasma confinement, on the other hand, are governed by the same type of equations [6]

$$\partial_t \nabla_{\perp}^2 \varphi + \{\varphi, \nabla_{\perp}^2 \varphi\} + g \partial_y p = \mu \nabla_{\perp}^4 \varphi, \quad (1)$$

$$\partial_t p + \{\varphi, p\} + R \partial_y \varphi = \kappa \nabla_{\perp}^2 p. \quad (2)$$

Here, $\nabla_{\perp}^2 = \partial_x^2 + \partial_y^2$ is the 2D nabla operator in the plane perpendicular to the external magnetic field. For both, 2DB as well as RGP, $\varphi(x, y, t)$ is the stream function, $\mathbf{v} = \hat{\mathbf{z}} \times \nabla \varphi$, which coincides with the scalar electric potential in the case of RGP. Furthermore, $p(x, y, t)$ is the temperature perturbation in the case of RB convection, or the pressure perturbation within the scope of RGP, respectively. The coefficients $\mu > 0$ and $\kappa > 0$ represent in both cases the viscosity and thermometric conductivity, respectively. The constants $R, g > 0$ are identified as the background density gradient and the magnetic field curvature in the case of RGP, or as the (instability driving) background temperature gradient and the gravity for the RB problem, respectively. Finally, $\{\cdot, \cdot\}$ denotes the Poisson bracket $\{F, G\} = (\partial_x F)(\partial_y G) - (\partial_y F)(\partial_x G)$. For RGP (RB convection) the radial (vertical) direction is identified as x and the poloidal (horizontal) direction as y .

The applicability of the 2D equations (1) and (2) to all features of actual RB-type experiments [8] or RGP may be questioned. For example, the flow in a Hele-Shaw cell, though effectively two dimensional, requires additional terms involving the drag of the confining plates to be taken into account. Other three-dimensional (3D) experimental setups, where instabilities of 2D initial conditions (convection rolls) are examined, clearly require a 3D discussion [9]. There is extensive literature available for 3D RB phenomena [10]. The situation is slightly different for RGP. In RGP, plasma motion along the magnetic field is considered as fast. Therefore, with good reasons, the situation can be approximated as 2D. Any inhomogeneity in the longitudinal direction is usually taken into account via an effective parallel wave number.

One should emphasize that magnetic shear and toroidicity effects are ignored in most (semianalytical) treatments mentioned so far. In the following we shall consider one of the

open questions within RGP, i.e., the existence of transport barriers in the presence of magnetic shear. Then, we shall generalize Eqs. (1), (2) to

$$\partial_t \nabla_{\perp}^2 \varphi + \alpha \{ \varphi, \nabla_{\perp}^2 \varphi \} = -s^2 \nabla_{\parallel}^2 \varphi - \alpha \partial_y p + \mu \nabla_{\perp}^4 \varphi, \quad (3)$$

$$\partial_t p + \alpha \{ \varphi, p \} = -\alpha \partial_y \varphi + \kappa \nabla_{\perp}^2 p. \quad (4)$$

Here, $\alpha = 2L_x/L_y$ is the (fluid) aspect ratio of the slab domain, and s^2 is the shear parameter. More details of the model (3), (4) are presented in Appendix A.

The boundary conditions (usually Dirichlet boundary conditions in x and periodic boundary conditions in y) require some clarification when comparing the results with experiments. In the y direction, the periodicity length L_y differs from $2\pi a$ (for a torus with minor radius a and major radius R_0), since on a poloidal cycle around the torus one passes both unfavorable and favorable curvature regions. Hence, strictly speaking, only on a fraction of $2\pi a$ the plasma configuration is Rayleigh-Taylor unstable at all. Having this in mind, the determination of the correct value of the periodicity length L_y is still an open problem, for both RB- and RGP-like applications.

Numerical simulations [7] of the shearless system (1) and (2), and semianalytical approaches using Galerkin approximations [6,8,11], have been used to unveil the bifurcation characteristics of the model. Note that, except for different normalization units, (1) and (2) are identical to (3) and (4) in the case $s \equiv 0$. It should be further mentioned that the works motivated by applications in plasma physics concentrated on codimension-1 bifurcations [for large (fluid) aspect ratios α]. There exist, however, interesting investigations [12] in fluid theory where codimension-2 bifurcations for small α are in the center of interest. We shall come back to this aspect later.

The celebrated Lorenz system [13] is probably the best known example for a physically motivated Galerkin approximation. In the present paper, using a Galerkin basis, our first aim is to clarify the codimension-1 bifurcation characteristics with respect to the (fluid) aspect ratio α . Note that the aspect ratio defined here contains a factor 2 compared to $\alpha_F := L_x/L_y$ as defined in some other related work [7,14,15]. The present definition is adopted from [6,8] and allows for a simpler mathematical notation. Using a more complete Galerkin description, even in the case $s \equiv 0$ an effect will be reported, which has not yet been discussed in the literature so far.

The second aim of the present paper is to investigate the influence of magnetic shear on the bifurcation scenario. Because of the then appearing explicit x dependence, simple Fourier modes in x cannot be adopted anymore. However, because of the ubiquitous presence of magnetic shear in magnetically confined plasmas, incorporation of shear is mandatory. We should note that besides α and s two other parameters, namely, μ and κ , are present in the system. They can be related to well-known parameters in fluid theory, namely, the Rayleigh number

$$\text{Ra} = \frac{\pi^4}{\mu \kappa} \quad (5)$$

and the Prandtl number

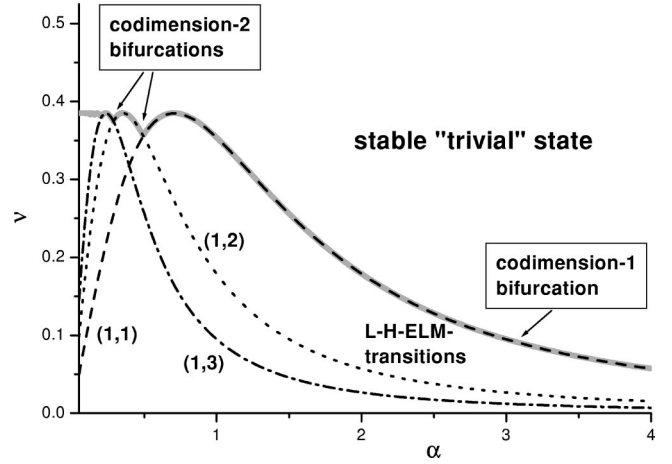


FIG. 1. Linear stability regions of Eqs. (3) and (4) for $\mu = \nu = \kappa$ and $s = 0$. In the (α, ν) plane, above the depicted curve $\nu = \nu(\alpha)$ the stable conductive states $\varphi = p = 0$ exist. The broken lines show the critical viscosity ν_{cr} for marginal stability in the shearless case ($s = 0$) for different linear modes [$\gamma_{l,m} = 0$ for $(l,m) = (1,1), (1,2), (1,3)$, respectively], as a function of the (fluid) aspect ratio α . For $\nu > \nu_{cr}$ the modes are linearly stable.

$$\text{Pr} = \frac{\mu}{\kappa}. \quad (6)$$

Instead of the Rayleigh number we shall use

$$\nu = \sqrt{\mu \kappa}. \quad (7)$$

The third aim of the present investigation is to point out the interesting dynamics that may appear near codimension-2 bifurcation points. In Fig. 1 we have summarized the regions of interest [for $\text{Pr} = 1$ and $s = 0$]. We are interested in the so-called “nontrivial” states that appear below a critical curve in the (α, ν) plane. As indicated by the broken lines [$\gamma_{l,m} = 0$ for $(l,m) = (1,1), (1,2), (1,3)$, respectively] of the figure, the critical curve is obtained as the envelope of the marginal stability curves for the linear modes. Besides results on the shear dependence of the so-called L-H-ELM transition region, we shall investigate the regions close to the codimension-2 bifurcation points where two linear modes become simultaneously unstable.

The present paper is organized as follows. Section II starts with a short description of the Galerkin approximation. Starting from a constant “trivial” (conductive) state, a codimension-1 bifurcation diagram with respect to the (fluid) aspect ratio α will be obtained and discussed for the shearless situation. We shall elaborate on the existence of a cutoff in α . It will be shown, however, that the cutoff disappears for reasonable magnetic shear. Section III presents an overview over the dynamical properties near the codimension-2 bifurcation points. It will be restricted, however, to effects up to third order in amplitudes. Section IV summarizes the results and concludes with a short outlook.

II. CODIMENSION-1 BIFURCATIONS, ASPECT RATIO, AND SHEAR DEPENDENCE

In this section we concentrate on the dynamics being dominated by one unstable mode. In other words, here we

investigate the lower right corner of Fig. 1. The shearless case is of special interest for fluid applications. Surprisingly enough, even in that simplified case some qualitatively new results follow from a detailed analysis.

Let us abbreviate (3) and (4) by

$$\partial_t \mathbf{H}\phi = \mathbf{L}\phi + \mathbf{N}(\phi, \phi), \quad (8)$$

where $\phi = (\varphi, p)^t$,

$$\mathbf{H} = \begin{pmatrix} -\nabla_{\perp}^2 & 0 \\ 0 & 1 \end{pmatrix}, \quad (9)$$

$$\mathbf{L} = \begin{pmatrix} s^2 \nabla_{\parallel}^2 & -\mu \nabla_{\perp}^4 & \alpha \partial_y \\ & -\alpha \partial_y & \kappa \nabla_{\perp}^2 \end{pmatrix}, \quad (10)$$

and \mathbf{N} represents the nonlinear term,

$$\mathbf{N}(\phi, \phi') = \alpha \begin{pmatrix} \{\varphi, \nabla_{\perp}^2 \phi'\} \\ \{\varphi, p'\} \end{pmatrix}. \quad (11)$$

As long as we concentrate on the shearless case we shall set $s=0$. We next introduce a truncated basis representation [16] in the form

$$\phi(x, y, t) \equiv \sum_{(l,m) \in \mathbf{B}} a_{lm}(t) \phi_{lm}(x, y). \quad (12)$$

While a complete expansion obviously describes the system exactly, the Galerkin approximation consists in selecting a finite subset \mathbf{B} of ‘‘relevant’’ modes (l, m) from the infinite basis functions. The index l is the radial label, whereas m is the toroidal wave number. Shear flow modes are naturally included as $(l, 0)$ modes. Real fields p and φ as well as the boundary conditions require that for each mode $(l, m) \in \mathbf{B}$ with $m \neq 0$ its conjugated mode $(l, -m)$ belongs to the Galerkin base, too. Within a Galerkin approximation we insert the truncated basis representation into the original partial differential equations. Projecting onto the (orthogonal) basis functions, we obtain closed (nonlinear) ordinary differential equations for the coefficients a_{lm} . The applicability of a Galerkin approximation for the present problem and its limitations can be deduced similar to previous investigations (e.g., [17]).

It is important to choose the appropriate modes. First, we can write ϕ_{lm} in the form ($p_{l0} = \varphi_{l0} = 0$)

$$\phi_{lm}(x, y) = \begin{pmatrix} -i \varphi_{lm}(x) \\ p_{lm}(x) \end{pmatrix} e^{imy}, \quad (13)$$

and relate the determination of φ_{lm} and p_{lm} to the linearized eigenvalue problem. The latter appears in the form

$$\gamma_{lm} \mathbf{H}_m \tilde{\phi}_{lm} = \mathbf{L}_m \tilde{\phi}_{lm}, \quad (14)$$

with the definitions

$$\mathbf{H}_m = \begin{pmatrix} -(\partial_x^2 - \alpha^2 m^2) & 0 \\ 0 & 1 \end{pmatrix}, \quad (15)$$

$$\mathbf{L}_m = \begin{pmatrix} -\mu(\partial_x^2 - \alpha^2 m^2)^2 - (s\alpha m x)^2 & -\alpha m \\ -\alpha m & \kappa(\partial_x^2 - \alpha^2 m^2) \end{pmatrix}. \quad (16)$$

Obviously,

$$\tilde{\phi}_{lm} = \begin{pmatrix} \varphi_{lm}(x) \\ p_{lm}(x) \end{pmatrix} \quad (17)$$

holds.

In the past, beginning with Lorenz [13], the understanding of the system (1) and (2) always leapt a step forward when the relevance of new modes (not included in prior work) was noticed (see [6,8,11]). In the present work we show that once again the system is richer than previously thought.

The first step in the analysis is the linearized case, i.e., we consider perturbations around the (‘‘trivial’’) conductive state. In the shearless situation, the analysis is quite straightforward, and a summary is presented in Appendix B. With magnetic shear, we obtain, of course, localized eigenfunctions. But there is no fundamental (qualitative difference) in determining the eigenvalue spectrum [18]; see also Appendix C.

A. Relevant modes

It is well known that the linear instability may saturate if μ and κ do not vanish. The saturation is achieved by the transport of energy (via nonlinearity) from the linearly growing modes to the small wavelengths (damping region). For simplicity, we will restrict ourselves here to the case $\text{Pr}=1$, i.e., $\nu = \kappa = \mu$.

The following behavior of the system (1) and (2) was reported in literature [6–8]: Starting from a purely conducting state, the system first undergoes a pitchfork bifurcation [19], when the viscosity is decreased below $\nu < \nu_{\text{cr}}(\alpha)$. Near the critical point, the first mode becomes linearly (Rayleigh-Taylor) unstable [that is the $(1, 1)$ mode for $\alpha > 0.493$; a shift to higher $(1, m)$ modes occurs below this aspect ratio; see the figure in Appendix B], and the system stays in the ‘‘Lorenz manifold’’ [8]. The instability saturates in a low (L) confinement state, which is characterized by an upright steady plumelike density perturbation and one (or more) vortex pair(s), see Figs. 2(a) and 2(b).

These vortex pairs are the typical trace of the Rayleigh-Taylor instability. If ν is further decreased, the L -state vortex becomes unstable via another supercritical stationary bifurcation, leaving the ‘‘Lorenz manifold.’’ Drake *et al.* [14] called that second instability a ‘‘peeling instability.’’ Shear flow is generated, which causes the vortex pair to tilt and saturate in a new steady state; see Figs. 2(c) and 2(d). According to the scenario presented in the literature, this so-called high confinement (H) mode appears when ν drops below $\tilde{\nu}_H(\alpha)$. The transition is accompanied by a reduction of the heat (particle) flux in the x direction and a transport barrier arises. For even lower ν values, $\nu < \tilde{\nu}_{\text{ELM}}(\alpha)$, the ‘‘peeling instability’’ eventually does not saturate in a pure H mode anymore. The ELM state [a (quasi-) periodic oscillating convection pattern] appears (see Fig. 3) via a supercritical Hopf bifurcation from the steady tilted cell. The (tilted) vortex pair is destroyed by shear flow generation. The

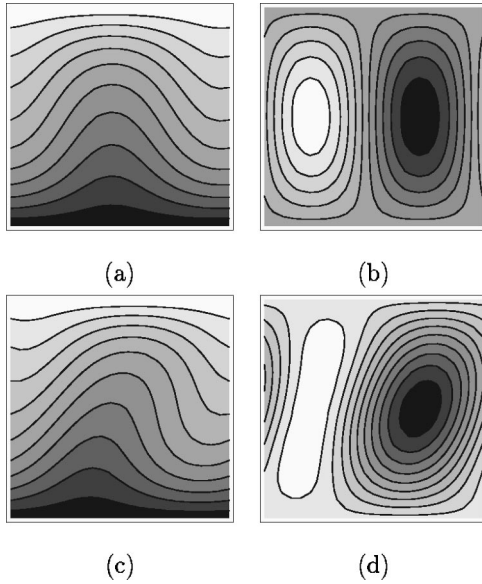


FIG. 2. Density profile (a) and potential (b) distribution of an L-mode saturated state for $\nu=0.16$ and $\alpha=2$ ($\alpha_F=1$). The same, (c), (d), for an H mode with $\nu=0.14$ and $\alpha=2$. Initial conditions are 0.1% random density perturbations. Here and in all the following graphs, the x axis points in the vertical direction and the y axis in the horizontal direction.

latter, in general, is too massive to let the system saturate in an H mode. Then the shear flow deteriorates, since all shear modes $(l,0)$ are linearly damped. Finally, the Rayleigh-Taylor instability once again forces the growth of a new vortex pair, and the cycle repeats. The graphs of $\tilde{\nu}_H(\alpha)$ and $\tilde{\nu}_{\text{ELM}}(\alpha)$, corresponding to the above scenario, are shown in Fig. 4.

Finn as well as Drake *et al.* [7,14,15] studied the influences of viscosity and (fluid) aspect ratio α on vortex stability first for a simplified vorticity equation model. Then, they extended their research to the full system (1) and (2). Using a low-dimensional Galerkin approximation, they considered the stability of a given vortex pair with respect to a small shear flow perturbation. Although this model might be a crude approximation to the real system dynamics (as it, in a way, considers shear flow generation but not vortex dynamics), the authors mention that there is a cutoff aspect ratio in the case of the “ideal” ($\nu \rightarrow 0$) peeling instability. In terms of the system (1) and (2), the inviscid instability is a rather degenerate situation since the (intermediate) saturation of a vortex can only take place when viscosity is present. The necessity arises to include both vortex and shear flow generation and their mutual coupling to understand the whole system. Earlier work by Howard and Krishnamurti [8] does not indicate the existence of a cutoff aspect ratio for the “tilted cell convection” (H mode). In the present paper we show that on the contrary, such a cutoff aspect ratio exists.

Our studies are also motivated by the question of whether the results of a Galerkin approximation are stable with respect to a supplementation of the Galerkin bases. Previously [8], the bases $\mathbf{B}=\{(1,1),(1,0),(2,\bar{0}),(2,1)\} \cup \{\text{conjugated modes}\}$ and an aspect ratio of $\alpha=1.2$ have been used. We found that there is one particular mode, the $(1,2)$ mode, which qualitatively changes the system dynamics. For small α , there are no more H or ELM states. Including the $(1,2)$

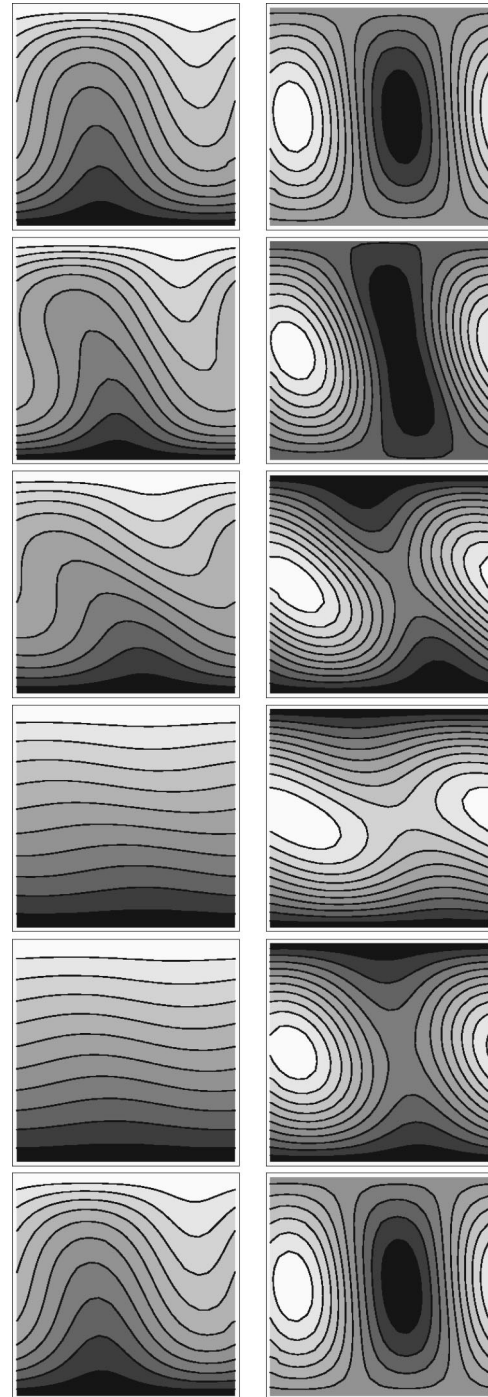


FIG. 3. Snapshots of the density profile (left column) and the potential (right column) of an ELM state for $\nu=0.12$ and $\alpha=2$ at times $t=107.0, 114.9, 120.2, 128.1, 133.4,$ and 141.3 , respectively (from top to bottom). At $t=144.0$ the cycle closes.

mode, the only visible result of the decrease in ν is a slight and steady change in the L-state shape of the density perturbation to more mushroomlike plumes (known from the Rayleigh-Taylor instability of fluids). Obviously, the $(1,2)$ mode prevents the energy to pile up in the $(1,0)$ φ shear mode and funnels it to linearly damped modes. It hence impedes the system in entering an H or ELM regime. There is no other mode like $(1,2)$, say, in the rectangular domain $(1,0), \dots, (5,5)$, that has this property. The “destructive nature” of the $(1,2)$ mode persists even if an arbitrary amount

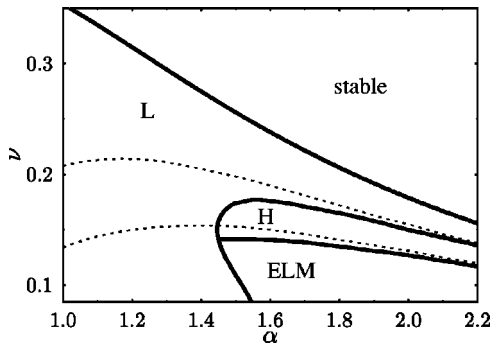


FIG. 4. Phase diagram for the existences of L, H, and ELM states (solid lines) with respect to aspect ratio α and viscosity ν for $s=0$ and fixed Prandtl number $\text{Pr}=1$. The dashed lines depict the border lines, which result from the truncation used in previous works.

of other modes (e.g., 100, which in resolution comes close to a direct numerical simulation) is included.

Evidently, the (1,2) mode plays a crucial role for the dynamics of the system, e.g., at an aspect ratio of 1.2. It hence should be taken into account when selecting a Galerkin base. The linear analysis presented in Appendix B gives an indication why the (1,2) mode may be as important as the other modes considered in the Galerkin base. At an aspect ratio of 1.2 the (1,2) mode becomes marginally unstable at a higher viscosity than the (2,1) mode, which is included in the set. With respect to linear instability the (1,2) mode is also more important than the shear modes, since the latter are always (linearly) damped. Hence, for a simulation one could employ a simple strategy to determine relevant modes from the linear growth rates. One should use the bases $\mathbf{G}_{\gamma^*}(\alpha, \nu, \text{Pr}) = \{(l, m) \in \mathbf{N} \times \bar{\mathbf{Z}} : \gamma_{lm}(\alpha, \nu, \text{Pr}) \geq \gamma^*\}$. The maximum value of γ^* should be fixed in a way that a decrease of γ^* (hence supplementation of the base) does not significantly change the results.

B. Aspect ratio and magnetic shear dependences

We now present the detailed aspect ratio dependence of the L-H transition in the Rayleigh-Bénard problem (1) and (2). We used a finite Galerkin basis (and confirmed the results by including more modes). In Fig. 4, in dependence of α and ν the phase diagram for the various confinement modes is shown. In the calculations leading to the solid lines in Fig. 4 we focused on viscosities $\nu > 0.1$. As a rule, lower viscosities always require a higher resolution, because the number of linearly unstable modes increases quadratically with $1/\nu$. With decreasing values of ν , the dissipative region is shifted to smaller scales, thus claiming for larger bases to model the system. Typically, viscosities $\nu \approx 0.1$ and below require bases with 100 or more modes.

We clearly see that for large values of α (> 1.6) the previous results (dashed lines) are confirmed. However, for small α (< 1.5) a significant deviation from previous predictions actually occurs: H and ELM states cease to exist for $\alpha < 1.45$. In addition, there is an ELM-L transition for $1.45 < \alpha < 1.53$ when ν is decreased sufficiently. The diagram displayed in Fig. 4 was obtained using large Galerkin bases. The qualitative features of the phase diagram remain for smaller bases, as long as the (1,2) mode is taken into ac-

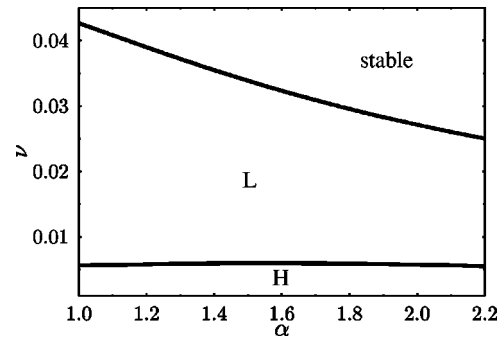


FIG. 5. Same as Fig. 4, but for $s=32/\pi$. Note that the H-ELM transition is not shown since it occurs very close to the $\nu=0$ axis.

count. It should be noted, however, that Fig. 4 only shows the L-H-ELM route; as will be discussed later, for smaller α values new characteristic states may appear.

In the case of magnetic shear the basic equations (3) and (4) become explicitly x dependent, and the eigenfunctions are not anymore harmonic in x . For the Galerkin approximation we recalculated the explicit forms of the eigenfunctions. Knowing the latter, we now proceed in a similar way as in the preceding section. Projecting on a finite Galerkin basis, we solve the ordinary differential equations to determine the bifurcation diagram in (ν, α) space. In Fig. 5 we show a typical example for $\text{Pr}=1$ and $s=32/\pi$. Note that the cutoff in α has disappeared, and the L-H transition occurs at much smaller ν values, compared to the shearless result (Fig. 4). The borderline for the H-ELM transitions appears at very small ν values (and therefore is not resolved in Fig. 5). This is understandable because of the effective shear damping. Moreover, at the bifurcation line many modes are linearly unstable in the strongly sheared situation. This is also significantly different from the shearless case. Going back to the definition of s , the value $s=32/\pi$ used for demonstration is easy to realize in experiments. In other words, with magnetic shear the L-H-ELM transition can be expected even for small (fluid) aspect ratios.

C. Codimension-1 and coupled mode approximations

The supercritical bifurcation to the L state can be analyzed in a rigorous mathematical manner by making use of center manifold theory (CMT) for codimension-1 bifurcations.

In its strict form, for codimension-1 problems, CMT [19,20] provides us with one amplitude equation for the (one) marginal mode at (α_c, ν_c) . The theory has been worked out in, e.g., [21], and the amplitude equation for the L state is

$$\partial_t x_1 = \gamma_1 x_1 + A_1^{111} |x_1|^2 x_1. \quad (18)$$

with explicitly known coefficients γ_1 and A_1^{111} . The present numerical treatment fully confirms the analytical predictions. The agreement is better the closer we are to the marginal (critical) curve shown in Fig. 1.

A generalization of the pure codimension-1 analysis was proposed in [22]. Besides the dominating unstable (1,1) mode, the driven (1,0) mode has been included in order to

incorporate a sheared poloidal flow. Shear flow generation via Reynolds stress can be investigated via

$$\partial_t x_0 = \gamma_0 x_0 + A_0^{01\bar{1}} x_0 |x_1|^2, \quad (19)$$

$$\partial_t x_1 = \gamma_1 x_1 - A_0^{001} x_0^2 x_1 + A_1^{11\bar{1}} |x_1|^2 x_1. \quad (20)$$

This is a physically motivated, but mathematically not rigorously justified treatment. It has been shown that besides the (1,2) mode (amplitude x_2), e.g., the (1,3) mode (amplitude x_3) and the (2,1) mode (amplitude x_4) alter the results. Then we get a system of five coupled ordinary differential equations [21]. This is a quite satisfactory analytical approximation to the numerical simulations. We can think of a nonlinearly modified damping $[\gamma_0 \rightarrow \gamma_0 + A_0^{01\bar{1}} |x_1|^2$ in case of the (1, 0) mode] and growth $[\gamma_1 \rightarrow \gamma_1 - A_1^{11\bar{1}} x_0^2$ in case of the (1, 1) mode] rates such that there may be a nonlinearly generated codimension-2 bifurcation point. The mathematically fully justified theory of such an extended (or renormalized codimension-2 bifurcation) analysis is however still missing. The main problem in formulating a rigorous codimension-2 theory for the L-H-ELM transition is due to the fact that we only approximately know the L and H states themselves. It should be mentioned that similar problems arise for the so-called nonlinear instabilities, which are of growing interest in many fields [23].

In Sec. III we shall present results from an exact codimension-2 analysis, in a parameter region where all the coefficients can be evaluated without approximations. For the present situation, in a first step, we verified the effect of the (1,2) mode by analytical studies of the L-state stability (with a 2×4 mode Galerkin approximation linearized around the L state), similar to the studies in [6,8]. Evaluating the linear stability using the Hurwitz criterion, the numerical results were confirmed.

III. THIRD ORDER THEORY FOR TWO UNSTABLE MODES

Now, we investigate regions where two modes become simultaneously unstable (upper left corner in Fig. 1). This analysis will show that the resistive- g paradigm is much richer than thought previously. Assuming $s=0$, two linearly independent marginal Fourier modes [wave vector $\mathbf{k} = (m, n)$, with $m \geq 1$ and $n \geq 0$ by convention] can be obtained. We are interested in those modes which become first unstable when dissipation (ν) is decreased, i.e., the (1, n) modes, for $n \in N$. Along their lines of marginality, the kernel of the linear operator is two dimensional (since there are two modes for each wave vector) everywhere except in points, where two curves intersect. The (α, ν) coordinates of these points with a four-dimensional kernel of \mathbf{L} and two simultaneously marginal wave vectors (1, n) and (1, $n+1$) are

$$\alpha = \frac{1}{n} \left(\frac{n}{n+1} \right)^{1/3} \left[\left(\frac{n+1}{n} \right)^{2/3} + 1 \right]^{-1/2}, \quad (21)$$

$$\nu = \frac{\left(\frac{n+1}{n} \right)^{1/3} + \left(\frac{n}{n+1} \right)^{1/3}}{\left[\left(\frac{n+1}{n} \right)^{2/3} + 1 + \left(\frac{n}{n+1} \right)^{2/3} \right]^{3/2}}. \quad (22)$$

We specialize for the pair (α, ν) with the highest possible α value, viz., $n=1$ and $(\alpha_c, \nu_c) \approx (0.4934, 0.3558)$. At this so-called critical (marginal) point, the linear, nonlinear, and energy operators are denoted by \mathbf{L}_c , \mathbf{N}_c , and \mathbf{H}_c , respectively. The kernel of \mathbf{L}_c is spanned by the eigenfunctions for the zero eigenvalue, Φ_1, \dots, Φ_4 , given by

$$\Phi_{2n-1} = N \begin{pmatrix} \frac{1}{q_n} \sin x \sin ny \\ -\sqrt{\text{Pr}} \sin x \cos ny \end{pmatrix}, \quad (23)$$

$$\Phi_{2n} = N \begin{pmatrix} \frac{1}{q_n} \sin x \cos ny \\ \sqrt{\text{Pr}} \sin x \sin ny \end{pmatrix}, \quad (24)$$

for $n=1,2$, where $N=2/(1+\text{Pr})^{1/2}$ is used as a normalization constant, and $q_n=(1+\alpha_c^2 n^2)^{1/2}$.

A. Amplitude equations

Within CMT, the bifurcation parameters $\Delta\nu = \nu - \nu_c$ and $\Delta\alpha = \alpha - \alpha_c$ are provided with trivial ‘‘equations of motion,’’ $\partial_t \Delta\nu = 0$ and $\partial_t \Delta\alpha = 0$, and treated as ‘‘marginal modes’’ with ‘‘synthetic eigenfunctions’’ Φ_5 and Φ_6 . CMT implies that near the marginal point the dynamics is dominated by the marginal modes; all other linear modes are said to be ‘‘slaved.’’ According to this, the temporal dependence of the complete field $\Phi(x, y, t)$ is expressed in terms of the amplitudes of the marginal modes $x_i(t)$ alone,

$$\Phi = \sum_{1 \leq i \leq 6} x_i \Phi_i + \sum_{1 \leq i \leq j \leq 6} x_i x_j \Phi_{ij} + \sum_{1 \leq i \leq j \leq k \leq 6} x_i x_j x_k \Phi_{ijk} + \dots \quad (25)$$

Here, the spatial expansion coefficients are given by the marginal modes $\Phi_i(x, y)$ in first order and unknown higher order contributions $\Phi_{ij}(x, y), \Phi_{ijk}(x, y)$, and so on. The latter summarize the influence of slaved modes. Apart from the amplitudes of the kernel modes, x_1, \dots, x_4 , the bifurcation parameters appear in a natural way among the amplitudes by defining $x_5 = \Delta\nu$ and $x_6 = \Delta\alpha$.

For the temporal evolution of the marginal mode amplitudes the ansatz

$$\partial_t x_i = \sum_{1 \leq j \leq 6} a_i^j x_j + \sum_{1 \leq j \leq k \leq 6} a_i^{jk} x_j x_k + \sum_{1 \leq j \leq k \leq l \leq 6} a_i^{jkl} x_j x_k x_l + \dots \quad (26)$$

is applied, where the coefficients a_i^j , etc., are to be determined. Because of the trivial equations of motion for the bifurcation parameters, we already know that all coefficients $a_5^{r, \dots, s}$ and $a_6^{r, \dots, s}$ vanish.

Finally the operators L , H , and N remain to be expanded in terms of x_i ,

$$L = L_c + (x_5 \partial_\nu + x_6 \partial_\alpha) L_c + \frac{1}{2} (x_5 \partial_C + x_6 \partial_\alpha)^2 L_c + \dots, \quad (27)$$

$$H = H_c + x_6 \partial_\alpha H_c + \dots, \quad (28)$$

$$N = N_c + x_6 \partial_\alpha N_c + \dots. \quad (29)$$

Inserting the expansions (25)–(29) into Eq. (8), we obtain a system of partial differential equations for the spatial expansion coefficients Φ_{ij} , Φ_{ijk} and so on, which is correct up to, e.g., the third order in x_i . In order to calculate the temporal evolution coefficients $a_i^{r,\dots,s}$, the system is treated in a two step process in ascending orders of x_i : By projecting the system on the marginal modes of the adjoined problem, the temporal evolution coefficients $a_i^{r,\dots,s}$ of the actual order are calculated. Then the equations are solved for the spatial expansion functions $\Phi_{i,\dots,m}$ of that order, which are required for the next step.

There are as many as 308 higher order (≥ 2) temporal evolution coefficients to be calculated for obtaining Eq. (26) in third order. It appears to be prudent to consider the implications of the symmetries of Eq. (8) on the evolution coefficients. They already reduce the number of coefficients to be calculated appreciably. In the present case we can make use of the $O(2) \times Z(2)$ symmetry group [24,25]. Specifically, all coefficients for quadratic terms of x_1, \dots, x_4 vanish. In complex notation $z_1 = x_1 + ix_2$ and $z_2 = x_3 + ix_4$, Eqs. (26) are condensed to

$$\partial_t z_1 = \gamma_1 z_1 + d_{11} |z_1|^2 z_1 + d_{12} |z_2|^2 z_1, \quad (30)$$

$$\partial_t z_2 = \gamma_2 z_2 + d_{21} |z_1|^2 z_2 + d_{22} |z_2|^2 z_2, \quad (31)$$

where

$$\gamma_1 = a_i^{i5} x_5 + a_i^{i6} x_6 + a_i^{i55} x_5^2 + a_i^{i56} x_5 x_6 + a_i^{i66} x_6^2, \quad (32)$$

$$\gamma_2 = a_j^{j5} x_5 + a_j^{j6} x_6 + a_j^{j55} x_5^2 + a_j^{j56} x_5 x_6 + a_j^{j66} x_6^2, \quad (33)$$

with $i = 1$ or 2 , $j = 3$ or 4 , and

$$d_{11} = a_1^{111} = a_1^{122} = a_2^{211} = a_2^{222}, \quad (34)$$

$$d_{12} = a_1^{133} = a_1^{144} = a_2^{233} = a_2^{244}, \quad (35)$$

$$d_{21} = a_3^{311} = a_3^{322} = a_4^{411} = a_4^{422}, \quad (36)$$

$$d_{22} = a_3^{333} = a_3^{344} = a_4^{433} = a_4^{444}. \quad (37)$$

All other coefficients (up to cubic order) vanish. Hence there are only 14 to be really calculated. In addition, the number of spatial expansion functions required in the explicit calculation is reduced to seven. Details are presented in Appendix D.

After having projected the dynamics of a rather complex system near the marginal point on a rather simple set of nonlinear ordinary differential equations (30) and (31), the discussion of these equations will reveal the nonlinear long time dynamics of the original system near the critical point.

The first step towards this goal is to transform the amplitude equations to normal forms. Equations (30) and (31) are easily transformed into a normal form by the polar ansatz $z_j = r_j \exp\{i\theta_j\}$, for $j = 1, 2$, which gives two coupled nonlinear differential equations for the radii. After a normalization $r_1' = r_1 |a_1^{111}|^{1/2}$, $r_2' = r_2 |a_3^{333}|^{1/2}$, we get

$$\partial_t r_1 = -r_1 (\mu_1 + r_1^2 + b r_2^2), \quad (38)$$

$$\partial_t r_2 = -r_2 (\mu_2 + c r_1^2 + r_2^2), \quad (39)$$

and two trivial evolution equations for the angles, $\partial_t \theta_j = 0$. In Eqs. (38) and (39) the primes were omitted and $\mu_j = -\gamma_j$, $b = -a_1^{133}/|a_3^{333}|$, $c = -a_3^{113}/|a_1^{111}|$ were defined. The equations constitute a normal form that was first discussed by Takens [26]. As has been mentioned already, besides the $O(2)$ symmetry, the $Z(2)$ symmetry applies here too. The latter causes the vanishing of the quadratic terms, which otherwise should be expected [12,27]. For a further discussion see also [28].

At this stage it is important to emphasize the difference to Eqs. (19) and (20). Although we again get two coupled equations, now other modes are coupled. The reason is that we are in a different parameter regime. Also the structure of the coupled equations (38) and (39) is not identical to that of Eqs. (19) and (20). Therefore, in the following we have to unveil the nonlinear dynamics associated with the model (38) and (39). At the first glance, that analysis will look very technical. However, at the end we shall detect a whole variety of fascinating possibilities, which may explain why (experimentally) very often physical systems do not react according to the simple L-H-ELM transition scenario.

B. Unfoldings

For all codimension-1 and some codimension-2 normal forms the so-called unfoldings, i.e., the classification of the nonlinear dynamics in terms of phase space portraits, are already known and discussed in literature, see, e.g., [19].

Extracting the phase portraits of Eqs. (38) and (39) requires the calculation of fixed points (r_1^* , r_2^*) and their linear stability: (spiral) source, sink, or saddle point. Then the flow topology can be reconstructed for the entire (r_1, r_2) phase space. The possible fixed points are presented in Table I together with their domains of existence. Fixed point 1 is the analog of the ubiquitous trivial solution. Fixed points 2 and 3 correspond to pure (1,1) or (1,2) mode states, respectively. Fixed point 4 denotes a mixed (1,1)-(1,2) state.

The domains of existence in Table I are given by relations between μ_1 and μ_2 , which are functions of the bifurcation parameters and the Prandtl number, and the coefficients b and c that are functions of the Prandtl number alone. For any value of Pr there are regions in the (α, ν) plane where all fixed points exist. Their linear stability however varies. Depending on the signs of b , c , and $1 - bc$, with $c > 0$ always, one can identify three different ‘‘cases.’’

Each case contains a set of six different regimes of unfoldings, which are delimited by the curves $\mu_1 = 0$, $\mu_2 = 0$, $\mu_1 = b\mu_2$, and $\mu_2 = c\mu_1$ in the (α, ν) plane. The last two curves, called pitchfork curves, indicate the boundaries of the domain of existence for the fixed point 4. They are re-

TABLE I. Four possible fixed points of systems (38) and (39).

Coordinates (r_1^*, r_2^*)	Domain of existence
fixed point 1 $(0,0)$	all μ_1, μ_2, b, c
fixed point 2 $(\sqrt{-\mu_1}, 0)$	all $\mu_1 \leq 0, \mu_2, b, c$
fixed point 3 $(0, \sqrt{-\mu_2})$	all $\mu_1, \mu_2 \leq 0, b, c$
fixed point 4 $(\sqrt{(b\mu_2 - \mu_1)/(1-bc)}, \sqrt{(c\mu_1 - \mu_2)/(1-bc)})$	all μ_1, μ_2, b, c with $(b\mu_2 - \mu_1)/(1-bc) > 0, (c\mu_1 - \mu_2)/(1-bc) > 0$

stricted to the region $\{(\alpha, \nu) : \mu_1 \leq 0 \text{ or } \mu_2 \leq 0\}$, i.e., where the fixed points 2 or 3 exist. The crossover of these curves signals changes in the flow topology, i.e., the fixed point existence and stability. The ‘‘crossing events’’ are related to the changes in sign of b and $1 - bc$ (c is always positive).

For $0 < Pr < 0.280691$, we have $b < 0$ and therefore $1 - bc > 0$. This is the so-called case III (the numbering is due to Takens’ original work [26]). Figure 6 exemplifies the six sectors of the $(\Delta\alpha, \Delta\nu)$ plane where different unfoldings are realized for case III using $Pr = 0.24$. The numbers 1, . . . , 8 refer to the different types of unfoldings, which are summarized in Fig. 7. The asterisks (‘‘4*’’ and ‘‘8*’’) indicate that the fixed point 4 in this unfolding is realized as a spiral source, whereas all other sources or sinks are ordinary ones otherwise. Topologically we do not have to distinguish between spiral and ordinary sources or sinks, anyway. It is however important to note that spirally attracting or repelling fixed points sometimes give rise to Hopf bifurcations, which are prone to considerably complicate the discussion. We can rule out Hopf bifurcations in our problem since there is no point in the (α, ν) plane where the stability related eigenvalues for the fixed point 4 are imaginary conjugates [19], i.e., where the fixed point changes its behavior from a spiral source to spiral sink or vice versa. The same holds for all other fixed points. As a result there are pitchfork bifurcations only. Later however, we will have to come back to this problem. It is then interesting that the type-8 unfolding, which shows a finite $(1, 1)$ mode contribution, exists in a region of phase space where this mode is linearly stable.

For $Pr \in [0.280691, 0.296461]$, we have $b > 0$ and still $1 - bc > 0$, giving the so-called case I(a). Coming from lower Prandtl numbers, the $\mu_1 = b\mu_2$ curve has crossed the $\mu_1 = 0$ line eliminating type 8 in favor of type-3 unfoldings. Figure 8 shows the bifurcation diagram for $Pr = 0.288$.

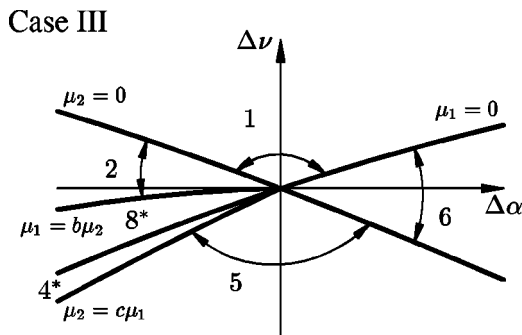


FIG. 6. The unfolding sectors for $Pr = 0.24$ are depicted in the $(\Delta\nu, \Delta\alpha)$ plane. The numbers 1 to 8 correspond to the types of unfoldings given in Fig. 7. The $\Delta\alpha$ axis range is -0.05 to 0.05 , the $\Delta\nu$ axis ranges from -0.03 to 0.03 .

With $Pr > 0.296461$, b remains positive but $1 - bc < 0$ changes sign, giving rise to case I(b). On route from case I(a) to I(b) the pitchfork curves $\mu_1 = b\mu_2$ and $\mu_2 = c\mu_1$ have crossed, switching the stability characteristics of the fixed point 4 from source to saddle point. Simultaneously, the fixed points 2 and 3 have become sources (cf. unfolding type 7) creating the only unfolding where two sources complete. Figure 9 exemplifies the case for $Pr = 1.5$. Further increase of the Prandtl number does not result in any more changes in sign, i.e., line crossovers.

All eight types of unfoldings in Fig. 7 eventually lead to saturated final states. The saturated states coincide with the sources in the phase space diagrams, i.e., the fixed points 1 through 4, depending on the Prandtl number and the unfolding parameters. They are unique except for the type-7 unfolding, where the system may either realize fixed point 2 or 3 as a final state (but not both together).

C. Comparison with numerical simulations

We checked our CMT results and their ranges of validity in the (α, ν) plane (which might be limited to a rather small neighborhood of the critical point) by comparing with direct numerical simulations.

In the previous section we discussed and finally denied the possibility of Hopf bifurcations for the fixed point 4, which is stable for the cases III and I(a), i.e., $Pr \leq 0.296461$. The numerics, in contrast, reveal that the fixed point actually becomes unstable to a so-called tertiary (pitchfork) bifurcation. This instability, however, occurs at a finite distance from the marginal point, indicating that it is a higher than third order phenomenon. In Fig. 10, an example for this instability is shown for $Pr = 0.24$. The bifurcation parameters $\Delta\alpha, \Delta\nu$ are decreased along the line $\Delta\nu = 0.2\Delta\alpha$, which is located in the type-8 unfolding sector. Theory predicts that there are three fixed points, 1, 3, and 4, with the first two of them unstable. Up to $\Delta\alpha \approx -0.01$ we have excellent agree-

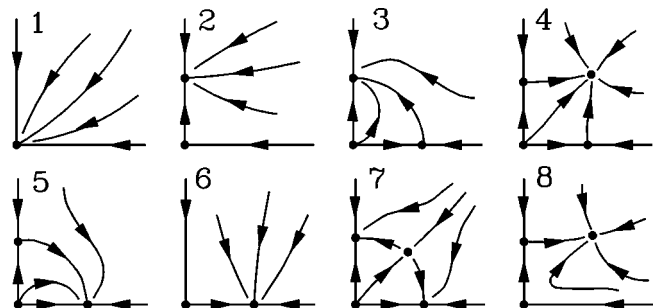


FIG. 7. The phase flows for the eight types of unfoldings. The horizontal axis depicts the r_1 coordinate, the vertical axis r_2 .

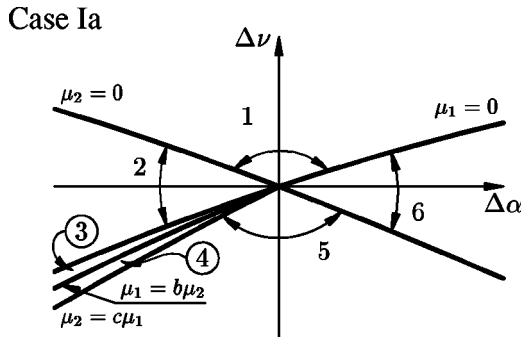


FIG. 8. Same as Fig. 6, but for $\text{Pr}=0.288$.

ment between theory and numerical simulation. With increasing distance from the origin, the (1,1) mode amplitudes fall short of the theoretically predicted values and begin to decrease. In parallel, the (1,2) mode amplitudes are enhanced to strengths well above the analytically calculated levels. For $\Delta\alpha \approx -0.016$ they eventually saturate at values that are in good agreement with a fixed point 3 saturated state, whereas the (1,1) mode amplitudes vanish. Clearly, an exchange of instability has taken place between the fixed points 4 and 3. The fixed point characteristics change from source to saddle point, and vice versa. Similar results were obtained for type-4 unfoldings in both cases I(a) and III (here, only for larger $|\Delta\alpha|$, $|\Delta\nu|$). On the other hand, we observed no such exchange process between the fixed points 4 and 2 (for type-4 unfoldings).

Tertiary bifurcations were found to be limited to situations with a stable fixed point 4. For other stable fixed points similar procedures like that outlined above did not show qualitative discrepancies like a tertiary bifurcation. Large distances from the origin only led to quantitative deterioration in the agreement of CMT and numerical results, e.g., for $\Delta\nu = -0.1$ [-0.2], the potential levels differ by approximately 2% [10%], but the pressure levels lie 30% [50%] lower than predicted. The increasing deviation can mainly be attributed to the inability of third order CMT to model the effective damping through energy cascades. However, in the numerical simulations third order CMT modes (Φ_i and Φ_{ij}) contain typically more than 98% of the systems total energy.

In order to demonstrate that the CMT results are in good agreement with numerical simulation data in a (small) neighborhood of the bifurcation point, we varied the bifurcation parameters along circles $(\Delta\nu, \Delta\alpha) = -\rho(\sin\theta, \cos\theta)$. On its way through the parameter space the system thus passes all different types of unfoldings that exist for a given case. Fig-

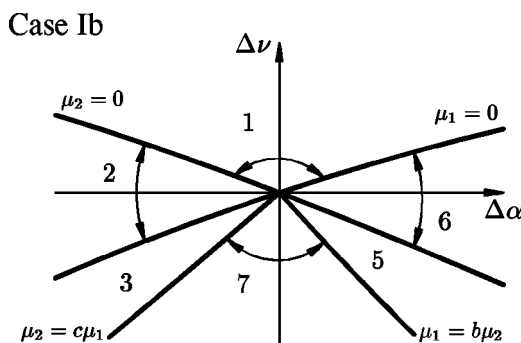


FIG. 9. Same as Fig. 6, but for $\text{Pr}=1.5$.

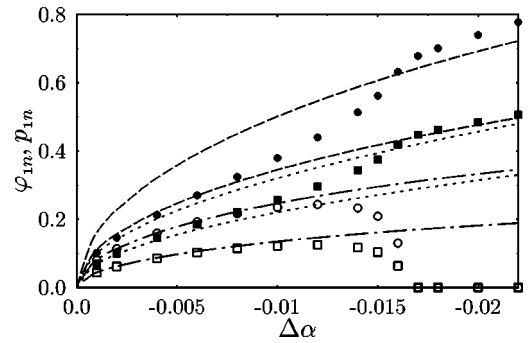


FIG. 10. Comparison of CMT predictions (lines) and a numerical experiment (symbols). Dashed lines represent fixed point 3 saturated (φ, p) states, dotted lines indicate (1,2), and dashed-dotted lines (1,1) (φ, p) components of the fixed point 4 saturated states, respectively. The φ curves always exceed the p curves. Solid symbols denote numerical (1,2) values, open symbols represent (1,1) components. φ values are denoted by circles, squares represent p values.

ure 11 shows the results for $\text{Pr}=1.5$ [case I(b)] with $\rho = 0.01$. The trivial, i.e., stable, part of the angular range was omitted. The numbers between the dotted vertical lines indicate the type of unfolding. Note that in Fig. 9 the lines (CMT predictions) indicate the existence of fixed points, but not its stability properties. Also the lines for the unstable fixed point 4 are not shown. To check the stability of both theoretically stable fixed points of the type-7 unfolding, we successfully tried to prepare the system in both possible saturated states. Which state is to be realized in a given situation depends on the initial conditions imposed. In these numerical simulations we started with a CMT approximated (unstable) fixed point 4 state. Figure 12 covers case I(a) ($\text{Pr}=0.288$) using $\rho = 0.002$. Again, the agreement between theory and numerical experiment is good, although the enlarged type-4 unfolding domain indicates the onset of the tertiary bifurcation. Figure 13 proves the validity of the CMT prediction for case III with $\text{Pr}=0.24$ and $\rho = 0.01$.

Stable fixed point 4 saturated states are clearly a result of nonlinear dynamics: When considering linear growth rates, the (1,2) mode is by far the dominant mode throughout all type-4 and -8 unfolding sectors of case III. When starting from random initial conditions, indeed a fixed point 3 saturated state emerges first. The system then slowly moves

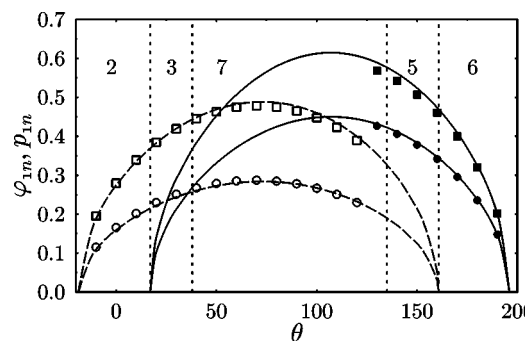
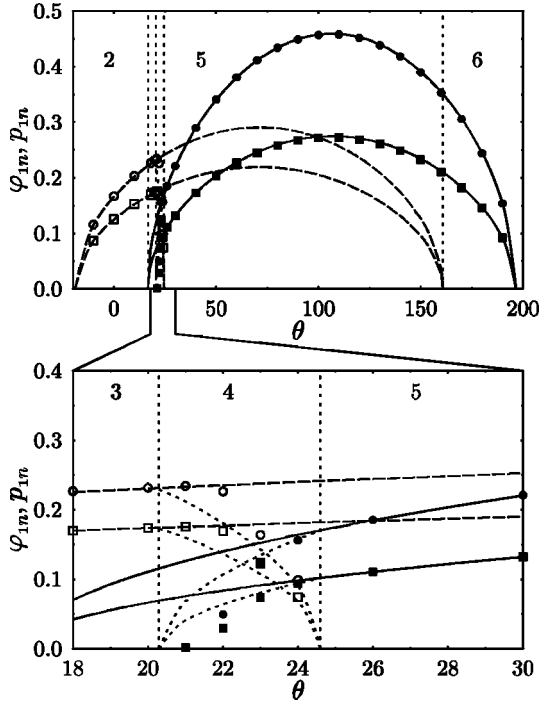
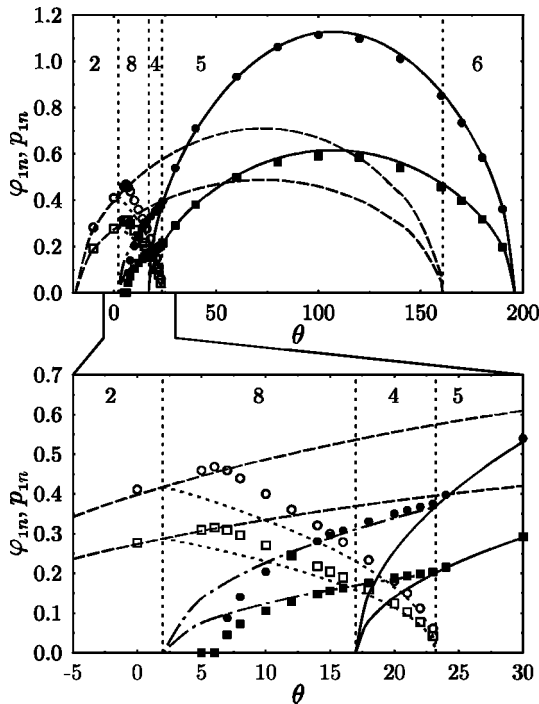


FIG. 11. Comparison of CMT prediction (lines) with numerical simulation (symbols) for $(\Delta\nu, \Delta\alpha) = -\rho(\sin\theta, \cos\theta)$, $\text{Pr}=1.5$, and $\rho = 0.01$. In addition to Fig. 10, solid lines denote fixed point 2 saturated (φ, p) states.

FIG. 12. Same as Fig. 11, but for $\text{Pr}=0.288$ and $\rho=0.002$.

along the unstable direction of fixed point 3 towards fixed point 4. Its amplitudes decrease to fixed point 4 levels, as, in turn, the (1,1) fields grow in magnitude. Except for the type 7 unfoldings of case Ib, we found that the final state of our numerical simulations did not depend on the initial conditions applied.

The present unfolding analysis is valid only up to third order in amplitude and in a small neighborhood of the origin ($|\Delta\alpha|, |\Delta\nu| \leq 0.01$). Because of the vanishing of all even orders in x_1, x_2, \dots , the relative phase remains undeter-

FIG. 13. Same as Fig. 11, but for $\text{Pr}=0.24$.

mined. The individual phases couple to the relative phase by a fifth order equation [28]. Also for the present case, an extension, by advancing the CMT to fifth order, is possible and will be published elsewhere.

IV. CONCLUSIONS

In the present paper the bifurcation behavior of the system (3) and (4) with respect to the (fluid) aspect ratio, viscosity, and magnetic shear has been analyzed. Three main results have been obtained. First, in the shearless case and for small (fluid) aspect ratios, the commonly accepted L-H-ELM transition scenario has been shown to need some refinement. Second, with increasing magnetic shear the cutoff in α disappears, and the L-H-ELM transition becomes the generic picture. Third, regions exist where the bifurcation scenario is much more complicated than reported previously.

ACKNOWLEDGMENTS

This work has been supported by the Deutsche Forschungsgemeinschaft through SFB 191 and the Graduiertenkolleg ‘‘Hochtemperatur-Plasmaphysik.’’

APPENDIX A: THE MODEL EQUATIONS

In the single helicity approximation, including magnetic shear and finite electric conductivity, the RGP equations (1) and (2) can be generalized. In dimensional form they appear as [21]

$$\partial_t \nabla_{\perp}^2 \varphi + c \{ \varphi, \nabla_{\perp}^2 \varphi \} = - \frac{4\pi v_A^2}{\eta c^2} \nabla_{\parallel}^2 \varphi - \frac{2g_0}{\rho_0} \partial_y p + \tilde{\mu} \nabla_{\perp}^4 \varphi, \quad (\text{A1})$$

$$\partial_t p + c \{ \varphi, p \} = - c p'_0 \partial_y \varphi + \tilde{\kappa} \nabla_{\perp}^2 p. \quad (\text{A2})$$

First, we note that for η (resistivity) $\rightarrow \infty$, we recover the simplified model (1) and (2). The following notations have been used: $v_A = B_0 / \sqrt{4\pi\rho_0}$ is the Alfvén velocity, depending on the toroidal magnetic field strength B_0 and the average mass density ρ_0 ; c is the velocity of light; $p'_0 = -\partial p_0 / \partial x > 0$ is the zeroth-order pressure gradient in slab geometry; $g_0 > 0$ characterizes the magnetic curvature and follows via $\mathbf{b}_0 \cdot (\mathbf{g} \times \nabla p) \approx -g_0 \partial_y p$ from the curvature vector $\vec{g} = (\vec{b} \cdot \vec{\nabla}) \vec{b}$.

The operator

$$\nabla_{\parallel} := \mathbf{b}_0 \cdot \vec{\nabla} \approx \partial_z + \frac{1}{R_0 q(r)} \partial_{\theta} \approx \partial_z - \frac{x}{L_s} \partial_y \quad (\text{A3})$$

has been defined. In its last form [as it appears on the right-hand side of (A3)] we have approximated ∇_{\parallel} in the vicinity of a magnetic surface situated at $r = r_0$. This is a quite standard procedure leading to the shear length L_s in the so-called slab geometry.

The single helicity approximation means that we only consider resonant modes (m, n) with $q(r_0) = m/n$. Here m and n are the azimuthal (poloidal θ) and longitudinal (toroidal ζ) wave numbers in the simplified (e.g., cylindrical) coordinate system. Note that because of magnetic shear the so-called q factor

$$q(r) \equiv \frac{\vec{B}_0 \cdot \vec{\nabla} \zeta}{\vec{B}_0 \cdot \vec{\nabla} \theta} \quad (\text{A4})$$

depends on radius r . In (local) slab geometry, the radial coordinate is denoted by x . Furthermore, within the slab geometry we choose the z direction in the direction of the actual magnetic field at $x=r_0$ (i.e., the z axis does not coincide anymore with the cylinder or ζ axis). Since the equilibrium is only x dependent, Fourier decompositions in θ and ζ (respectively, y and z) are possible, with the remarkable result

$$e^{i(m\theta+n\zeta)} \rightarrow e^{i\{my/r_0 + [n-m/q(r_0)]z/R_0\}} \quad (\text{A5})$$

to lowest order in r_0/R_0 . That means that within the single helicity approximation the z dependence becomes negligible, and on the resonant surface $q(r_0)=m/n$ we can approximate

$$\nabla_{\parallel}^2 \approx \left(\frac{x}{L_s}\right)^2 \partial_y^2. \quad (\text{A6})$$

Choosing the origin of the x axis at the point corresponding to $r=r_0$, we consider x to vary within $[-d, d]$. That means that $L_x=2d$ is the extension in the x direction. Dirichlet boundary conditions are assumed in x , i.e.,

$$\varphi(\pm d, y, z, t) = \nabla_{\perp}^2 \varphi(\pm d, y, z, t) = p(\pm d, y, z, t) = 0. \quad (\text{A7})$$

On the other hand, periodic boundary conditions are demanded for $0 \leq y \leq L_y \approx 2\pi r_0$, e.g.,

$$\varphi(x, 0, z, t) = \varphi(x, L_y, z, t), \quad (\text{A8})$$

and so on.

As a natural length scale we introduce

$$\xi = \frac{2d}{\pi}. \quad (\text{A9})$$

The Rayleigh-Taylor growth rate induces the natural time scale

$$\tau = \sqrt{\frac{\rho_0}{2g_0 \rho_0' r_0}}. \quad (\text{A10})$$

Normalizing

$$\frac{\varphi c \tau}{\xi^2} \rightarrow \varphi, \quad p_0' \xi p \rightarrow p, \quad \mu = \frac{\tilde{\mu} \tau}{\xi^2}, \quad \kappa = \frac{\tilde{\kappa} \tau}{\xi^2}, \quad (\text{A11})$$

$$x/\xi \rightarrow x, \quad \alpha y/\xi \rightarrow y, \quad z/L_s \rightarrow z, \quad (\text{A12})$$

and introducing the shear parameter

$$s^2 = \frac{4\pi v_A^2 \xi^2 \tau}{\eta c^2 L_s^2}, \quad (\text{A13})$$

we finally end up with the following nondimensional system

$$\partial_t \nabla_{\perp}^2 \varphi + \alpha \{ \varphi, \nabla_{\perp}^2 \varphi \} = -s^2 \nabla_{\parallel}^2 \varphi - \alpha \partial_y p + \mu \nabla_{\perp}^4 \varphi, \quad (\text{A14})$$

$$\partial_t p + \alpha \{ \varphi, p \} = -\alpha \partial_y \varphi + \kappa \nabla_{\perp}^2 p, \quad (\text{A15})$$

where

$$\nabla_{\parallel} = \partial_z - \alpha x \partial_y \approx -\alpha x \partial_y, \quad \nabla_{\perp}^2 = \partial_x^2 + \alpha^2 \partial_y^2. \quad (\text{A16})$$

The independent variables vary within

$$(x, y, z) \in \left[-\frac{\pi}{2}, \frac{\pi}{2} \right] \times [0, 2\pi] \times \left[0, \frac{2\pi R_0}{L_s} \right]. \quad (\text{A17})$$

As in standard fluid theory we call

$$\alpha = \frac{4d}{2\pi r_0} \triangleq \frac{2L_x}{L_y} \quad (\text{A18})$$

the (fluid) aspect ratio of the slab domain. This definition should not be confused with the standard definition of the aspect ratio of a tokamak.

APPENDIX B: LINEAR STABILITY ANALYSIS IN THE SHEARLESS CASE

Starting from a (conductive) state $\varphi=p=0$, linear analysis of the system (3,4) yields for $s \equiv 0$ to the growth rate

$$\gamma_{lm}^{\pm} = -\frac{\nu}{2} \frac{1 + \text{Pr}}{\sqrt{\text{Pr}}} k_{lm}^2 + \left[\frac{\nu^2}{4} \frac{(1 - \text{Pr})^2}{\text{Pr}} k_{lm}^4 + \frac{\alpha^2 m^2}{k_{lm}^2} \right]^{1/2} \quad (\text{B1})$$

for a mode with $k_{lm}^2 = l^2 + \alpha^2 m^2$. If either μ or κ vanishes, all modes become linearly unstable, whereas for positive μ , κ there is a finite number of unstable modes, and short wavelengths are damped. The linearly most unstable mode (l^*, m^*) always has $l^* = 1$, since γ_{lm} decreases monotonically with increasing l . Its wave number $m^* \geq 1$ varies like $\alpha m^* = f(\nu)$, where $f(\nu)$ is a lengthy expression, which does not merit being given explicitly here. We have $f(\nu) \sim O(1)$ for $\nu \in [0.1, 0.3]$. The critical ($\gamma=0$) viscosities $\nu_{cr}(\alpha; l, m) = \alpha m (l^2 + \alpha^2 m^2)^{-3/2}$ are plotted by the broken lines [$\gamma_{l,m}=0$ for $(l, m) = (1, 1), (1, 2), (1, 3)$, respectively] of Fig. 1 for various modes.

The corresponding eigenfunctions are

$$\tilde{\phi}_{lm}^{\pm}(x) = \frac{1}{N_{lm}^{\pm}} \begin{pmatrix} -[\nu k_{lm}^2 \text{Pr}^{-1/2} + \gamma_{lm}^{\pm}] / \alpha m \\ 1 \end{pmatrix} f_l(x), \quad (\text{B2})$$

where

$$f_l(x) = \begin{cases} \sin(lx) & \text{for } l \text{ even,} \\ \cos(lx) & \text{for } l \text{ odd.} \end{cases} \quad (\text{B3})$$

N_{lm}^{\pm} is the normalization constant.

For $m=0$, φ and p decouple (in the linear limit), and we introduce the notation $m=0, \bar{0}$ with

$$\tilde{\phi}_{l0}(x) = \frac{\sqrt{2}}{l} \begin{pmatrix} 1 \\ 0 \end{pmatrix} f_l(x), \quad (\text{B4})$$

$$\tilde{\phi}_{l0}(x) = \sqrt{2} \begin{pmatrix} 0 \\ 1 \end{pmatrix} f_l(x). \quad (\text{B5})$$

The corresponding damping rates are $\gamma_{l0} = -\nu\sqrt{\text{Pr}}l^2$ and $\gamma_{l\bar{0}} = -\nu l^2/\sqrt{\text{Pr}}$, respectively.

APPENDIX C: LINEAR STABILITY ANALYSIS IN THE SHEARED CASE

In general, in the presence of magnetic shear, the eigenvalue spectrum has to be determined numerically. For the understanding of the dependencies, it is quite instructive to go to a limit where the growth rates and eigenfunctions can be determined analytically. We first note that we can completely eliminate the parameter s in the basic equations by the following changes of variables:

$$xs \rightarrow x, \quad ys \rightarrow y, \quad s^2\varphi \rightarrow \varphi, \quad sp \rightarrow p, \quad (\text{C1})$$

leaving t and z unchanged, and replacing $s^2\mu \rightarrow \mu$ and $s^2\kappa \rightarrow \kappa$. Then, in the basic equations (3) and (4), the parameter s disappears, but of course the size of the system (L_x, L_y) as well as the dissipation parameters become s dependent. For a physical discussion it is more instructive to keep the effect of resistivity via s , and to introduce only the new variable X via

$$X^2 = \frac{s\alpha|m|}{\gamma^{1/2}} x^2. \quad (\text{C2})$$

For $\mu = \nu = 0$ the linear eigenvalue problem can then be transformed into a standard form. Some simple manipulations lead to

$$\partial_X^2 \varphi + \left[\frac{\alpha|m|}{s} \frac{1-\gamma^2}{\gamma^{3/2}} - X^2 \right] \varphi = 0, \quad (\text{C3})$$

i.e., the standard equation for Hermite polynomials $H_n(X)$. Note that for large s we have practically the infinite domain $[-\infty, +\infty]$, and the eigenfunction solutions can be written in the forms

$$\varphi(X) \approx e^{-X^2/2} H_{l-1}(X), \quad l \in N. \quad (\text{C4})$$

The corresponding eigenvalues follow from

$$s^{-1}\alpha|m|(1-\gamma^2)\gamma^{-3/2} = 2l-1. \quad (\text{C5})$$

The asymptotically valid expressions approximate very well the numerical ones.

For the eigenvalues γ we can investigate two limits. First, when

$$\Delta_{lm} := \frac{(2l-1)s}{\alpha|m|} \gg 1, \quad (\text{C6})$$

i.e., for small m , we find $\gamma \rightarrow 0$ and therefore

$$\gamma \approx \frac{1}{(\Delta_{lm})^{2/3}} \sim s^{-2/3} \sim \eta^{1/3}, \quad (\text{C7})$$

i.e., the well-known scaling for resistive interchange modes.

On the other hand, for

$$\Delta_{lm} \rightarrow 0, \quad (\text{C8})$$

i.e., very high m modes leading to $\gamma \rightarrow 1$, the growth rate no longer depends on the resistivity.

APPENDIX D: CALCULATION OF SOME COEFFICIENTS

Let us introduce a scalar product that can be used to project on the marginal modes. The projection can be thought of as solvability conditions which the partial differential equations for Φ_i, Φ_{ij} , etc, are required to fulfill. These conditions impose that the inhomogeneity, i.e., everything but $L_c\Phi_i, L_c\Phi_{ij}$, and so on, is orthogonal to the kernel of the adjointed operator of L_c . Denoting the scalar product by $\langle \cdot, \cdot \rangle$ we define

$$\langle \Phi, \Phi' \rangle = \frac{1}{(2\pi)^2} \int_{-\pi/2}^{\pi/2} \int_0^{2\pi} (\varphi\varphi' + pp') dx dy. \quad (\text{D1})$$

It is readily verified that the operator L_c is self-adjointed with respect to $\langle \cdot, \cdot \rangle$. Hence the marginal modes of the adjointed problem coincide with those of the original problem. The energy operator H_c ($\langle \Phi, H\Phi \rangle$ is twice the total energy of the system) is self-adjointed, too, and positive definite, which enables us to introduce a second scalar product $\langle \cdot, H_c \cdot \rangle$. The normalization constant N in (23) and (24) was chosen in a way that the marginal modes Φ_1, \dots, Φ_4 are orthonormal with respect to the second scalar product: $\langle \Phi_i, H_c \Phi_j \rangle = \delta_{ij}$, for $i, j = 1, \dots, 4$.

Implementing the strategy outlined in the main text, our calculation yields $a_i^j = 0$ for all i, j , and $\Phi_5 = \Phi_6 = (0, 0)'$ in first order. Second order coefficients are calculated from

$$a_m^{ij} = \langle \Phi_m, (\partial_{x_i} L_c) \Phi_j \rangle + \frac{1}{1 + \delta_{ij}} \langle \Phi_m, N_c(\Phi_i, \Phi_j) + N_c(\Phi_j, \Phi_i) \rangle, \quad (\text{D2})$$

giving

$$a_1^{15} = -2q_1^2 \frac{\sqrt{\text{Pr}}}{1 + \text{Pr}}, \quad a_1^{16} = 2 \frac{1 - 2\alpha_c^2}{q_1^3} \frac{\sqrt{\text{Pr}}}{1 + \text{Pr}}, \quad (\text{D3})$$

$$a_3^{35} = -2q_2^2 \frac{\sqrt{\text{Pr}}}{1 + \text{Pr}}, \quad a_3^{36} = 4 \frac{1 - 8\alpha_c^2}{q_3^2} \frac{\sqrt{\text{Pr}}}{1 + \text{Pr}}. \quad (\text{D4})$$

Next, we proceed with the second order spatial expansion functions Φ_{ij} and calculate the third order temporal evolution coefficients. Evaluating

$$a_m^{ijk} = \frac{1}{1 + \delta_{ik}} \langle \Phi_m, N_c(\Phi_i, \Phi_{jk}) + N_c(\Phi_{jk}, \Phi_i) + N_c(\Phi_j, \Phi_{ik}) + N_c(\Phi_{ik}, \Phi_j) \rangle \quad (\text{D5})$$

for $j, k \leq 4$, and

$$a_m^{ijk} = \frac{1}{1 + \delta_{jk}} \langle \Phi_m, \partial_{x_j} \partial_{x_k} L_c \Phi_i + \partial_{x_j} L_c \Phi_{ik} + \partial_{x_k} L_c \Phi_{ij} - a_i^{ik} H_c \Phi_{ij} - a_i^{ij} H_c \Phi_{ik} - a_i^{ij} \partial_{x_k} H_c \Phi_i - a_i^{ik} \partial_{x_j} H_c \Phi_i \rangle \quad (\text{D6})$$

for $j, k > 4$, yields, e.g.,

$$a_1^{111} = -\frac{\alpha_c q_1}{2} \frac{\text{Pr}^{3/2}}{(1+\text{Pr})^2}, \quad (\text{D7})$$

$$a_3^{333} = -\alpha_c q_2 \frac{\text{Pr}^{3/2}}{(1+\text{Pr})^2}, \quad (\text{D8})$$

$$a_1^{133} = \frac{0.065271 + 0.021308 \text{Pr} - 0.904356 \text{Pr}^2}{\sqrt{\text{Pr}(1+\text{Pr})^2}}, \quad (\text{D9})$$

$$a_3^{113} = -\frac{0.085379 + 0.064846 \text{Pr} + 0.932975 \text{Pr}^2}{\sqrt{\text{Pr}(1+\text{Pr})^2}}, \quad (\text{D10})$$

$$a_1^{155} = \frac{q_1^5 (1-\text{Pr})^2 \sqrt{\text{Pr}}}{\alpha_c (1+\text{Pr})^3}, \quad (\text{D11})$$

$$a_1^{156} = -2\sqrt{\text{Pr}} \frac{(1-\text{Pr})^2 + 8\alpha_c^2 \text{Pr}}{\alpha_c (1+\text{Pr})^3}, \quad (\text{D12})$$

$$a_1^{166} = \sqrt{\text{Pr}} [(1-\text{Pr})^2 - \alpha_c^2 (9 + 2 \text{Pr} + 9 \text{Pr}^2) + 2\alpha_c^4 (1 - 6 \text{Pr} + \text{Pr}^2)] [\alpha_c q_1^5 (1+\text{Pr})^3]^{-1}, \quad (\text{D13})$$

$$a_3^{355} = \frac{q_2^5 (1-\text{Pr})^2 \sqrt{\text{Pr}}}{2\alpha_c (1+\text{Pr})^3}, \quad (\text{D14})$$

$$a_3^{356} = -2\sqrt{\text{Pr}} \frac{(1-\text{Pr})^2 + 32\alpha_c^2 \text{Pr}}{\alpha_c (1+\text{Pr})^3}, \quad (\text{D15})$$

$$a_3^{366} = 2\sqrt{\text{Pr}} [(1-\text{Pr})^2 - 4\alpha_c^2 (9 + 2 \text{Pr} + 9 \text{Pr}^2) + 32\alpha_c^4 (1 - 6 \text{Pr} + \text{Pr}^2)] [\alpha_c q_2^5 (1+\text{Pr})^3]^{-1}. \quad (\text{D16})$$

Due to lack of space we refrain from presenting exact expressions for a_1^{133} and a_3^{113} , which are complicated functions of α_c . Three nonlinear coefficients of the kernel modes (a_1^{111} , a_3^{333} , and a_3^{113}) are always negative, but a_1^{133} is only negative for Prandtl numbers greater than 0.280691.

-
- [1] B. B. Kadomtsev, *Tokamak Plasma: A Complex Physical System* (IOP, London, 1992).
- [2] P. G. Drazin and W. H. Reid, *Hydrodynamic Stability* (Cambridge University Press, Cambridge, 1981).
- [3] H. R. Strauss, *Phys. Fluids* **19**, 134 (1976).
- [4] B. B. Kadomtsev and O. B. Pogutse, *Zh. Eksp. Teor. Fiz.* **65**, 575 (1973) [*JETP* **38**, 283 (1973)].
- [5] H. Sugama and M. Wakatani, *J. Phys. Soc. Jpn.* **57**, 2010 (1988); **59**, 3937 (1990).
- [6] W. Horton, G. Hu, and G. Laval, *Phys. Plasmas* **3**, 2912 (1996).
- [7] J. M. Finn, *Phys. Fluids B* **5**, 415 (1992).
- [8] L. N. Howard and R. Krishnamurti, *J. Fluid Mech.* **170**, 385 (1986).
- [9] R. M. Clever and F. H. Busse, *J. Fluid Mech.* **65**, 625 (1974).
- [10] M. C. Cross and P. C. Hohenberg, *Rev. Mod. Phys.* **65**, 851 (1993), and references therein.
- [11] J. H. Curry, *Commun. Math. Phys.* **60**, 193 (1978).
- [12] D. Armbruster, J. Guckenheimer, and P. Holmes, *Physica D* **29**, 257 (1988).
- [13] E. N. Lorenz, *J. Atmos. Sci.* **20**, 130 (1963).
- [14] J. F. Drake, H. M. Finn, P. Guzdar, V. Shapiro, V. Shevchenko, F. Waelbroeck, A. B. Hassam, C. S. Liu, and R. Sagdeev, *Phys. Fluids B* **4**, 488 (1992).
- [15] J. M. Finn, J. F. Drake, and P. N. Guzdar, *Phys. Fluids B* **4**, 2758 (1992).
- [16] J.-L. Thiffeault and W. Horton, *Phys. Fluids* **8**, 1715 (1996).
- [17] M. Berning and K. H. Spatschek, *Phys. Plasmas* **5**, 2525 (1998).
- [18] B. A. Carreras, L. Garcia, and P. H. Diamond, *Phys. Fluids* **30**, 1388 (1987).
- [19] J. Guckenheimer and P. Holmes, *Nonlinear Oscillations, Dynamical Systems, and Bifurcations of Vector Fields* (Springer, New York, 1983).
- [20] J. Carr, *Applications of Centre Manifold Theory* (Springer, New York, 1981).
- [21] P. Beyer and K. H. Spatschek, *Phys. Plasmas* **3**, 995 (1996).
- [22] P. H. Diamond, X.-M. Liang, B. A. Carreras, and P. W. Terry, *Phys. Rev. Lett.* **72**, 2565 (1994).
- [23] K. Itoh, S.-I. Itoh, and A. Fukuyama, *Transport and Structural Formation in Plasmas* (IOP, Bristol, England, 1999), and references therein.
- [24] D. H. Sattinger, *J. Funct. Anal.* **28**, 58 (1978).
- [25] M. Shearer and I. C. Walton, *Stud. Appl. Math.* **65**, 85 (1981).
- [26] F. Takens, *Publ. Math. IHES* **43**, 47 (1974).
- [27] R. Grauer, *Physica D* **35**, 107 (1989).
- [28] D. Armbruster, *Physica D* **27**, 433 (1987).